

QUANTITATIVE ESTIMATES OF MINIMUM CORE MASSES FOR GIANT PLANET FORMATION **PAPER I** **WAS QUANTITATIVE.**

ANA-MARIA A. PISO
 Harvard-Smithsonian Center for Astrophysics

ANDREW N. YODIN
 JILA, University of Colorado at Boulder

RUTH A. MURRAY-CLAY
 Harvard-Smithsonian Center for Astrophysics
Draft version November 19, 2013

ABSTRACT

The core accretion model postulates that giant planets form through gas accretion onto a solid core. To accumulate a massive atmosphere, this core’s mass must exceed a minimum value M_{crit} often quoted as $10M_{\oplus}$. The value of M_{crit} , however, depends on the rate at which planetesimals accrete onto the core and heat its atmosphere. In this study we calculate the minimum core mass for atmospheric collapse in the limiting regime in which core growth is halted and the luminosity evolution of a core’s atmosphere is dominated by Kelvin-Helmholtz contraction. We build on the idealized model of Piso & Youdin (submitted), which derives the evolution of atmospheres accreting around protoplanetary cores and calculates the minimum (or critical) core mass to form a gas giant before disk dissipation. We enhance this model by employing a more realistic equation of state and dust opacity. We find that M_{crit} increases by more than a factor of two when non-ideal effects such as hydrogen dissociation and quantum rotation are included in the equation of state, when compared to an ideal gas polytrope. Lower opacities due to grain growth reduce M_{crit} . Taken together, we calculate $M_{\text{crit}} \sim 7M_{\oplus}$ at 5 AU, decreasing to $\sim 4.5M_{\oplus}$ at 100 AU, for a realistic EOS and a grain size distribution $n \propto a^{-3.5}$ with a maximum particle size of 1 cm. If $n \propto a^{-2.5}$, appropriate for coagulation, M_{crit} is up to one order of magnitude smaller. We show that giant planets may grow from smaller cores if core growth is halted, which is particularly relevant for understanding the origin of gas giants directly imaged at wide separations.

1. INTRODUCTION

Core accretion — a prominent theory of giant planet formation — stipulates that Jupiter-sized planets form when planetesimal accretion produces a solid core large enough to attract a massive atmosphere (e.g., Mizuno et al. 1978, Stevenson 1982, Bodenheimer & Pollack 1986, D’Angelo et al. 2011). Because protoplanetary disks dissipate on timescales of a few Myrs, cores must grow quickly to accrete disk gas. Forming large cores is particularly challenging in the outer disk, where long dynamical times slow core growth.

An *in situ* solution to this problem requires accelerating core growth to rates larger than those typically assumed, but fast growth produces an additional difficulty. Though the minimum, or critical, core mass to form a giant planet is typically quoted to be $M_{\text{crit}} \sim 10M_{\oplus}$, the actual value depends on how quickly planetesimals accrete (e.g., Ikoma et al. 2000, Pollack et al. 1996, Rafikov 2006). Fast accretion heats a core’s atmosphere, increasing pressure support and hence M_{crit} . However, planetesimal accretion rates need not be constant over time. If accretion slows before the nebular gas dissipates, the target M_{crit} for successful giant planet formation is substantially reduced.

In order to calculate the minimum value of M_{crit} , we first need to understand how M_{crit} depends on the plan-

etesimal accretion rate. For high planetesimal accretion rates, atmospheres are primarily heated by planetesimals (e.g., Rafikov 2006). As a result, the core’s envelope is in a steady state at all times, in which all the incoming energy due to planetesimals is radiated away. As the envelope and core become comparable in mass, hydrostatic balance no longer holds and runaway gas accretion commences. In this case, M_{crit} is the maximum core mass for which the atmosphere is still in hydrostatic equilibrium. For a fixed planetesimal accretion rate and a set of disk conditions, M_{crit} is uniquely determined.

However, planetesimal accretion rates need not be constant at a given location in the protoplanetary disk throughout the disk’s lifetime — in particular, planetesimal accretion may significantly reduce as the planet’s feeding zone is depleted of solids. Time-dependent core accretion models (e.g., Pollack et al. 1996, Ikoma et al. 2000) take this into account and include variable planetesimal accretion rates which allow for the Kelvin-Helmholtz (KH) contraction of the gaseous envelope to become important. In this regime, the envelope is no longer in a steady state, but rather it accretes gas as it cools. Pollack et al. (1996) find that the evolution of a giant planet can be separated into three phases. The core forms during phase 1 due to runaway planetesimal accretion, while the envelope mass stays small. Once the planet’s feeding zone has been depleted of solids,

planetesimal accretion is significantly reduced and can no longer balance radiative losses. As a result, the atmosphere cools while undergoing KH contraction; this is phase 2. The envelope mass now steadily increases while core growth is stalled. Runaway gas accretion begins once the atmosphere mass is comparable to the core mass in phase 3. Pollack et al. (1996) find that phase 2 lasts much longer than phases 1 and 3, and so the evolutionary timescale of the planet is set by KH contraction.

It is not clear *a priori* which of the two regimes — atmosphere evolution dominated by planetesimal accretion versus KH contraction — is the most relevant, as the conclusion of Pollack et al. (1996) depends on their assumptions about planetesimal accretion history. In particular, a core’s feeding zone may be replenished by migration of solids through the protoplanetary disk. In this study, we accept the three-stage growth, in which the core is fully formed before it accumulates a significant atmosphere. During the slow phase of atmospheric growth we thus assume that the luminosity of the envelope is only due to KH contraction and neglect ongoing planetesimal accretion. Our results yield lower core masses than studies that assume large planetesimal accretion rates, confirming that it may indeed be easier to grow a giant planet from a fully formed core. Moreover, as additional heating due to accretion of solids limits the envelope’s ability to cool and thus increases the core mass required for collapse, our results give a robust minimum for the core mass needed to form a giant planet before disk dissipation.

We follow the model developed in Piso & Youdin (submitted; hereafter Paper I) and consider quasi-static two-layer atmospheres, embedded in the protoplanetary disk. Paper I calculates the minimum (critical) core mass to form a gas giant at several locations in the protoplanetary disk. We build on the results of Paper I by making two important additions: we include realistic equation of state (EOS) effects, as well as realistic dust opacities.

Paper I assumes that the nebular gas is ideal, diatomic and can be described by a polytropic equation of state (EOS). However, non-ideal effects such as dissociation and ionization have to be taken into account in order to obtain better quantitative results. In this study, we consider atmosphere growth assuming a realistic gas with an EOS prescribed by the Saumon et al. (1995) tables.

Another simplified assumption of Paper I is that the dust opacity in radiative regions is that of interstellar grains. In reality, opacities in protoplanetary disks, while not tightly constrained observationally, are unlikely to be interstellar. In particular, grain growth and dust settling — which is particularly relevant to our regime of low planetesimal accretion in which solids have been segregated from the gas and are not being added back in — lower the opacity. In this study, we use realistic opacity tables that are calculated based on observations of protoplanetary disks and take into account grain growth.

This paper is organized as follows. In Section §2 we review the quasi-static and cooling models derived in Paper I. We discuss the variations in the adiabatic gradient caused by the non-ideal EOS in Section §3, and their effect on atmosphere evolution in Section §4. We determine the minimum core mass to form a giant planet during the disk lifetime in Section §6, with realistic EOS and dust opacity assumptions. In Section §7 we compare

our results to those obtained by studies that consider planetesimal accretion as the dominant source of energy. Finally, we summarize our findings in Section §8.

2. MODEL REVIEW

We begin by reviewing the model developed in Paper I for the structure and evolution of a planetary atmosphere embedded in a protoplanetary disk. We describe the assumptions of the model and the properties of our assumed protoplanetary disk in §2.1, and we summarize the equations describing the structure and time evolution of the atmosphere in §2.2.

2.1. Assumptions and Disk Model

We assume that the planet consists of a solid core of fixed mass and a two-layer atmosphere composed of an inner convective region and an outer radiative zone that matches smoothly onto the disk. The two regions are separated by the Schwarzschild criterion for convective instability (see §2.2). We denote the surface between the two regions as the radiative-convective boundary (RCB), defined by a radius $r = R_{\text{RCB}}$. Moreover, we assume that the luminosity is constant throughout the outer radiative region (see Section §6 for additional discussion). We assume a low planetesimal accretion regime in which the atmosphere evolution is dominated by KH contraction. The atmosphere is spherically symmetric, self-gravitating and in hydrostatic balance. We note that spherical symmetry confines us to the outer regions of the disk ($a \gtrsim 5$ AU), where the disk scale height is larger than the radius at which the planet matches onto the disk (see Paper I for further details). The nebular gas is composed of a hydrogen-helium mixture, with hydrogen and helium mass fractions of 0.7 and 0.3, respectively. We assume that the envelope evolves through stages of quasi-static equilibrium.

The temperature and pressure at the outer boundary of the atmosphere are given by the nebular temperature and pressure. As a disk model, we use the minimum mass, passively irradiated model of Chiang & Youdin (2010). The surface density, mid-plane temperature and mid-plane pressure are given by

$$\Sigma_d = 2200 (a/\text{AU})^{-3/2} \text{ g cm}^{-2} \quad (1a)$$

$$T_d = 120 (a/\text{AU})^{-3/7} \text{ K} \quad (1b)$$

$$P_d = 110 (a/\text{AU})^{-45/14} \text{ dyn cm}^{-2}, \quad (1c)$$

with a the semimajor axis and for a mean molecular weight $\mu = 2.35$.

2.2. Structure Equations and Cooling Model

The structure of a static atmosphere is described by the standard equations of hydrostatic balance and thermal equilibrium:

$$\frac{dP}{dr} = -\frac{Gm}{r^2}\rho \quad (2a)$$

$$\frac{dm}{dr} = 4\pi r^2\rho \quad (2b)$$

$$\frac{dT}{dr} = \nabla \frac{T}{P} \frac{dP}{dr} \quad (2c)$$

$$\frac{dL}{dr} = 4\pi r^2\rho(\epsilon + \epsilon_g), \quad (2d)$$

where r is the radial coordinate, P , T and ρ are the gas pressure, temperature and density, respectively, m is the mass enclosed by the radius r , L is the luminosity from the surface of radius r , and G is the gravitational constant. The gas is heated at a rate of $\epsilon_g \equiv -T \frac{ds}{dt}$ per unit mass due to gravitational contraction, where s is the specific gas entropy, while ϵ represents the rate at which internal heat is generated per unit mass. We do not take into account any internal energy sources and set $\epsilon = 0$. The temperature gradient $\nabla \equiv \frac{d \ln T}{d \ln P}$ depends on whether energy is transported throughout the atmosphere by radiation or convection. In the case of radiative diffusion for an optically thick gas, the temperature gradient is

$$\nabla = \nabla_{\text{rad}} \equiv \frac{3\kappa P}{64\pi G m \sigma T^4} L, \quad (3)$$

with σ the Stefan-Boltzmann constant and κ the dust opacity. In our models the atmosphere is optically thick throughout the outer boundary. Where energy is transported by convection, the temperature gradient is

$$\nabla = \nabla_{\text{ad}} \equiv \left(\frac{d \ln T}{d \ln P} \right)_{\text{ad}}, \quad (4)$$

with ∇_{ad} the adiabatic temperature gradient. The convective and radiative layers of the envelope are separated by the Schwarzschild criterion (e.g., Thompson 2006): the atmosphere is stable against convection when $\nabla < \nabla_{\text{ad}}$ and convectively unstable when $\nabla > \nabla_{\text{ad}}$. Since convective energy transport is highly efficient, $\nabla \approx \nabla_{\text{ad}}$ in convecting regions. The temperature gradient is thus given by $\nabla = \min(\nabla_{\text{ad}}, \nabla_{\text{rad}})$.

The Equation set (2) is supplemented by an equation of state (EOS) relating pressure, temperature and density, as well as an opacity law. Paper I assumes an ideal gas polytropic EOS, $P = K\rho^\gamma$, with K the adiabatic constant and γ the adiabatic index. In this study we use realistic EOS tables, as explained in Section §3. Furthermore, Paper I assumes a power-law opacity given by

$$\kappa = 2F_\kappa \left(\frac{T}{T_{\text{ref}}} \right)^\beta, \quad (5)$$

with β and F_κ constants, and T_{ref} a normalizing temperature. Paper I sets $\beta = 2$, $F_\kappa = 1$ and $T_{\text{ref}} = 100$ K, appropriate for ice grains in the interstellar medium (ISM) (Bell & Lin 1994). However, these values are valid only for low disk temperatures, $T_d \lesssim 100$ K, where all dust components are present. Furthermore, dust settling and grain growth lower both the normalization factor F_κ and the power-law coefficient β . In this paper, we explore more realistic opacity laws and their effect on the

critical core mass when compared to the ISM power-law, as discussed in Section §5.

We assume that the atmosphere forms around a solid core of fixed mass M_c with a radius $R_c = (3M_c/4\pi\rho_c)^{1/3}$, where ρ_c is the core density. We choose $\rho_c = 3.2$ g cm $^{-3}$ (e.g., Papaloizou & Terquem 1999). The atmosphere matches onto the protoplanetary disk at the Hill radius $R_H \equiv a \left(\frac{M_p}{3M_\odot} \right)^{1/3}$, where M_p is the total planet mass, $M_p = M_c + M_{\text{atm}}$. The Hill radius is the distance from the planet at which the gravitational attraction of the planet and the tidal gravity due to the host star are equal. Outside the Hill sphere, stellar tides unbind gas from the planet. The effective outer boundary of the atmosphere is the surface defined by the Bondi radius, $R_B \equiv \frac{GM_p}{c_s^2} = \frac{GM_p}{\mathcal{R}T_d}$. This is the distance from the planet at which the thermal energy of the nebular gas is of the order of the gravitational energy of the planet. Here c_s is the isothermal sound speed and \mathcal{R} is the reduced gas constant: $\mathcal{R} = k_B/(\mu m_p)$, with k_B the Boltzmann constant and m_p the proton mass. For $R_B < R_H$, several studies assume that the atmosphere matches onto the disk at R_B (e.g., Ikoma et al. 2000, Pollack et al. 1996). We choose the Hill radius as the outer boundary because the temperature and pressure at R_H are those of the disk, $T(R_H) = T_d$ and $P(R_H) = P_d$. Outside R_B , gas flows no longer circulate the planet, but rather belong to the disk. However, the density structure between R_B and R_H remains spherical and is still well described by hydrostatic balance (Ormel 2013). The flows outside R_B could affect the atmosphere's cooling; however, we expect this effect to be weak, as heat losses predominantly occur deep in the planetary atmosphere. This justifies our outer boundary choice. We note, however, that we define the planet mass as the mass enclosed inside the smaller of R_B or R_H .

Lastly, we review the cooling model developed in Paper I, used to determine the time evolution of the atmosphere between subsequent static models. A protoplanetary atmosphere embedded in a gas disk satisfies the following cooling equation:

$$L = L_c + \Gamma - \dot{E} + e_{\text{acc}}\dot{M} - P_M \frac{\partial V_M}{\partial t}. \quad (6)$$

Here, L is the total luminosity, L_c is the luminosity from the solid core, which may include planetesimal accretion and radioactive decay, and Γ is the rate of internal heat generation. We set $L_c = \Gamma = 0$. The \dot{E} term is the rate at which total energy (internal and gravitational) is lost, and e_{acc} is the specific total energy brought in by gas accreting at the rate \dot{M} : $e_{\text{acc}} = u - GM/R$, where u is the internal energy per unit mass. Finally, the last term represents the work done on a surface mass element.

We obtain an evolutionary series for the atmosphere by connecting sets of subsequent static atmospheres through the cooling Equation (6). Details of our numerical procedure are described in Paper I.

3. ADIABATIC GRADIENT FOR THE TABULATED EQUATION OF STATE

In order to describe the nebular gas, we use the interpolated EOS tables of Saumon et al. (1995) for a helium

mass fraction $Y = 0.3$, and extend them to lower temperatures and pressures corresponding to the conditions in our fiducial disk. Appendix A describes our extension procedure.

For an ideal gas polytropic EOS, the adiabatic gradient is constant. In contrast, non-ideal effects such as dissociation or ionization produce temperature-dependent variations in ∇_{ad} . Figure 1 shows a contour plot of the adiabatic gradient (defined in Equation 4) as a function of gas temperature and pressure. We distinguish three separate temperature regimes:

1. Intermediate temperature regime ($300 \text{ K} \lesssim T \lesssim 2000 \text{ K}$), where the hydrogen-helium mixture behaves like an ideal gas with a polytropic EOS.
2. High temperature regime ($T \gtrsim 2000 \text{ K}$), where dissociation of molecular hydrogen occurs, followed by ionization of atomic hydrogen for $T \gtrsim 10,000 \text{ K}$.
3. Low temperature regime ($T \lesssim 300 \text{ K}$), where the rotational states of the hydrogen molecule are not fully excited.

We note that helium behaves like an ideal monatomic gas with $\nabla_{\text{ad}} = 2/5$ in our regime of interest. Its presence in the atmosphere thus only causes a small, constant upward shift in the adiabatic gradient of the mixture.

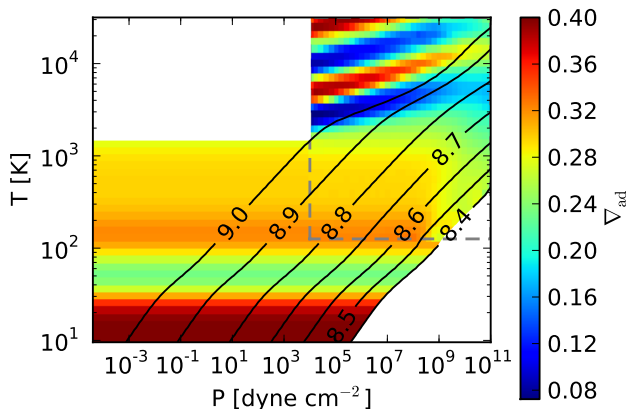


FIG. 1.— Contour plot of the adiabatic gradient ∇_{ad} for a hydrogen-helium mixture as a function of gas temperature and pressure. The upper-right rectangle encloses the region described by the original Saumon et al. (1995) EOS tables, while the rest of the plot is our extension. The black curves represent constant entropy adiabats, with the labels $\log_{10}(S)$ [erg K $^{-1}$ g $^{-1}$]. The regions in which the EOS is either invalid or not computed are masked in white. Our extension is only valid for $T \lesssim 2000 \text{ K}$, since it does not take into account hydrogen dissociation. We choose $T = 1500 \text{ K}$ as a conservative temperature cutoff. Saumon et al. (1995) do not compute the EOS at very high pressures, since hydrogen is solid or may form a Coulomb lattice in this regime, and thus their EOS treatment is no longer valid. While the boundaries of the region in which the free-energy EOS treatment fails can be determined from fundamental thermodynamic constraints, such calculations are not the object of this work. Instead, we choose as boundary a constant entropy curve ($\log(S) = 8.4$) above the region in which the Saumon et al. (1995) model fails. The expressions derived in Appendix A are sufficient to give good results for the colored regions of the extended map, which fully cover the temperature and pressures ranges required by our models. **This caption is extremely long. I would find a way to defer much of this to text.**

1. Intermediate T: Ideal Gas

For $300 \text{ K} \lesssim T \lesssim 2000 \text{ K}$, the hydrogen molecule is not energetic enough to dissociate and hydrogen behaves as an ideal diatomic gas with constant ∇_{ad} (Figure 1). The helium component of the gas causes a slight increase in the adiabatic index: $\nabla_{\text{ad}} \approx 0.3$ in this temperature range rather than $2/7$ as is the case for a diatomic gas¹.

2. High T: Dissociation and Ionization of Hydrogen.

At low temperatures, hydrogen exists in molecular form and has a stable configuration. As the temperature becomes higher than $T \sim 2000 - 3000 \text{ K}$, the internal energy of the hydrogen molecule becomes large enough to break the covalent bond between the atoms, and hydrogen starts dissociating. At $T \gtrsim 10,000 \text{ K}$, hydrogen ionizes. In stellar and giant planet interiors there is little overlap between the two processes: hydrogen is almost entirely dissociated into atoms by the time ionization becomes important.

As displayed in Figure 1, the adiabatic gradient decreases significantly in regions of partial dissociation and partial ionization. This behavior is different than that of a mixture of molecular and atomic hydrogen, for which $2/7 < \nabla_{\text{ad}} < 2/5$, or a mixture of protons and electrons, for which $\nabla_{\text{ad}} = 2/5$. For a mixture of ideal gases, the total internal energy is given by the sum of the internal energies of the individual gases. When a gas dissociates, however, part of the internal energy of the system is used to break down molecules, which reduces the amount of energy available to increase the temperature of the system, thus lowering the adiabatic gradient. The energy required to dissociate depends on the dissociation fraction, which can be determined from the Saha equation (see e.g., Kippenhahn & Weigert 1990). The dissociation fraction only depends on gas temperature and density, and hence only on the EOS.

An expression for the adiabatic gradient as a function of the dissociation fraction is presented in Appendix B.1. As expected, the adiabatic gradient is $\nabla_{\text{ad}} = 2/7$ for pure molecular hydrogen and $\nabla_{\text{ad}} = 2/5$ when hydrogen is fully dissociated, but decreases significantly during partial dissociation and is smallest when half of the gas is dissociated. This is consistent with the behavior we see in Figure 1.

The ionization of atomic hydrogen is also dictated by the Saha equation, with the dissociation energy replaced by ionization energy, hence the adiabatic gradient behaves analogously, consistent with Fig. 1.

3. Low T: Hydrogen Rotation and Spin Isomers

As a diatomic molecule, hydrogen has five degrees of freedom, three associated with translational motion and two associated with rotation. The excitation temperature for rotation is $\Theta_r \approx 85 \text{ K}$ (Kittel et al. 1981), hence the rotational states are fully excited at room temperature. As the gas temperature becomes comparable to Θ_r , fewer rotational states are excited, and rotation entirely ceases as $T \rightarrow 0$. We note that at temperatures larger than $\gtrsim 6000 \text{ K}$, vibrational motions also become

¹ Recall $\nabla_{\text{ad}} \equiv \frac{\gamma-1}{\gamma}$ for an ideal gas, with γ the adiabatic index: $\gamma = 7/5$ for a diatomic gas and $5/3$ for a monatomic gas.

important. While at $T \lesssim 2000$ K, where our extension of the Saumon et al. (1995) EOS tables is valid, vibrational motion is negligible, we include these effects in our extension of the EOS for completion (see Appendix A for details).

Molecular hydrogen occurs in two isomeric forms, parahydrogen and orthohydrogen. Parahydrogen has antiparallel proton spins and thus an antisymmetric wave function. From the Pauli exclusion principle it follows that it can only occupy symmetric rotational states with even angular quantum number j (Farkas 1935). In contrast, orthohydrogen has parallel proton spins and a symmetric wave function, and can therefore only occupy states with odd j . At equilibrium, the relative abundance of the ortho- and para- states is given by the ratio of their partition functions, described in Appendix A. At $T \rightarrow 0$ all hydrogen molecules are in the ground state with $j = 0$, which corresponds to parahydrogen. As the temperature increases, parahydrogen starts converting into orthohydrogen, resulting in an ortho-para equilibrium ratio of 3:1 at room temperature.

Similarly to the case of dissociation, as T increases, part of the rotational energy U_r of the hydrogen molecule is used to convert parahydrogen to orthohydrogen rather than to only increase the temperature, so $U_r \propto T$ no longer holds. The adiabatic gradient ∇_{ad} thus varies with temperature. Appendix B.2 explores the temperature dependence in detail. These ∇_{ad} variations, which occur for $T \lesssim 300$ K, are displayed in Figure 1. At higher temperatures, the ortho-para 3:1 equilibrium ratio is reached; no further isomer conversion occurs, and thus ∇_{ad} remains relatively constant until dissociation temperatures are reached.

4. EQUATION OF STATE EFFECTS ON ATMOSPHERE EVOLUTION LONG SECTION TITLE. JUST "ROLE OF EOS"?

Variations in the adiabatic gradient ∇_{ad} due to partial dissociation and quantum ('Quantum' is not a useful descriptor (IMO). All EOS effects are quantum, noting molecular or H_2 rotation would be more descriptive.) rotational effects (see §3) have two competing (Not 'competing,' both contribute and can/do go in same direction) effects on the atmospheric evolution of a core's atmosphere. Putting the equation $\dot{M} = -L/(dE/dM)$ early in the explanation would help. They yield: (1) a lower envelope luminosity, and (2) a larger amount of radiated energy per unit of accreted mass, when compared to an ideal gas. Both effects A bit confusing if you mean EOS effects or resulting evolution effects. Maybe avoid reusing 'effects'.) combined slow down accretion and increase the growth time of the atmosphere and thus the critical core mass.

In what follows it may be clearer to start with the motivation: isolating the two EOS effects, i.e. dissociation and rotation. Then introduce the two patched EOSs as how we do this. Currently it's less clear and more drawn out where this is going.

In order to explain how quantum rotational states at low temperatures affect atmospheric growth, we perform

the following thought experiment (I don't see how this is a thought experiment, or why we have to imagine. I would just describe the EOSs): we imagine that the EOS deviates from a polytrope only in the upper atmosphere where temperatures are low, and that the gas is ideal and polytropic deep in the envelope. Conversely, we study the effects of dissociation at high temperatures by assuming that the EOS is realistic at the bottom of the atmosphere where temperatures are high, but that the gas is polytropic in the outer regions. **Finish the description of the EOSs first. Then describe and interpret Fig. 2 starting in a new paragraph. Starting the fig description at the end of a methods discussion lost me.)** Figure 2 shows the time evolution of atmospheres forming at 10 AU around cores of mass $M_c = 10M_\oplus$ and described by various equations of state, as follows:

I would make this list numbered and omit the reference to the curve styles, which is clear in figures.

- Dashed curve (1) — ideal gas polytrope with $\nabla_{\text{ad}} = 0.3$.
- Dotted curve (2) — ideal gas polytrope with $\nabla_{\text{ad}} = 0.3$ for $T > 500$ K and realistic EOS for $T < 500$ K.
- Dash-dotted curve (3) — ideal gas polytrope with $\nabla_{\text{ad}} = 0.3$ for $T < 500$ and realistic EOS for $T > 500$ K.
- Solid curve (4) — fully realistic EOS. (Here and elsewhere, I don't like "fully" realistic, as it implies a perfect EOS. I would just say realistic at all T .)

We choose $T = 500$ K as the cutoff temperature because the hydrogen-helium mixture behaves like an ideal gas, with $\nabla_{\text{ad}} = 0.3$, in this temperature regime (see Figure 1). (I find the references to curve numbers distracting in general. I would try to do less of this and focus on describing the physical effects. The reader still needs to look at the figure, and there the curves are clearly labelled.) As such, the time evolution difference between curves (1) and (2) shows the quantum rotational effects on the atmosphere evolution, while the difference between curves (1) and (3) accounts for hydrogen dissociation. We see that both dissociation and rotational states have a comparable effect (due to log scale, I would not call the effects comparable, just b/c they go in same direction) on the atmosphere growth and result in slower cooling. The growth time is dependent on both the total energy that must be released (i.e., the rate at which energy is released) and on the luminosity of the atmosphere. 'Rate of energy release' and luminosity are the same thing. You may be calling dE/dM a 'rate' which is confusing. Again, I think if you introduce and physically explain $\dot{M} = -L/(dE/dM)$ at the outset, then the resulting explanations can more compactly and clearly refer to the terms that matter. We explore the relative influence of these two factors separately. Haven't you already started exploring these factors separately? Why say this again?

Also perhaps worth a note (if not an explanation) that the combined effect is significantly greater than either individually (again noting log scale).

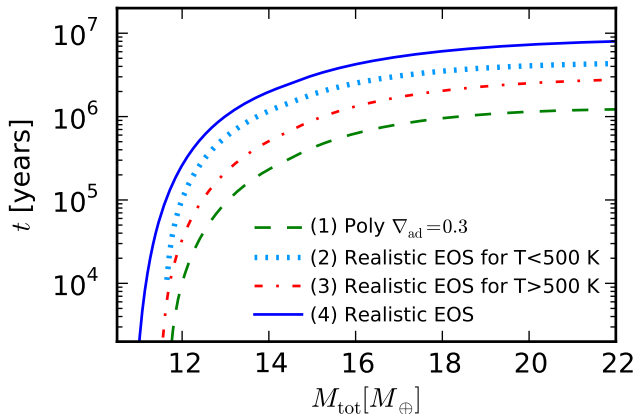


FIG. 2.— Elapsed time to grow a planet of total mass (core + atmosphere) for a variety of EOS combinations (see text), for a planet forming at 10 AU and with a fixed core mass $M_c = 10M_\oplus$. Both hydrogen dissociation at high temperatures deep in the atmosphere and quantum rotational effects at low temperatures in the outer envelope result in slower cooling when compared to an ideal gas polytrope.

The upper-right panel of Figure 3 shows the luminosity evolution with mass for atmospheres (1)–(4) ~~our model EOSs~~, for an ~~example core with $M_c = 10M_\oplus$ core forming~~ (as core isn't forming, this phrase is misleading in addition to being too lengthy) at 10 AU. We see that the lower luminosity of the fully realistic EOS (4) when compared to the polytrope (1) is due to the realistic EOS in the outer atmosphere (2). This behavior is directly correlated to the depth of the radiative region of the envelope, which is shown in the upper-left panel of Figure 3 for a total planet mass of $12M_\oplus$. We see that the realistic EOS for low temperatures (2) results in a deeper location of the RCB when compared to the ideal gas polytrope (1). **This is an accurate observation. The deeper question is why does the EOS change result in a deeper RCB? This should be possible to understand, right?** This deeper RCB translates into a larger number of steps that photons need to diffuse to escape from the RCB, and therefore a lower luminosity (cf. Equation 3). **Better to just say it's an optical depth effect than reexplaining how radiative diffusion works. Also it's the pressure depth (not the radius) that correlates more closely with optical depth. A plot of $P(r)$ might thus help as noted in fig caption.**

Dissociation deep in the planet's atmosphere increases the amount of energy per unit mass that needs to be radiated by the envelope, which further slows down growth. **Why is this true? Dissociation absorbs energy which by itself decreases the amount of energy that needs to be radiated.** Figure 3, lower-left plot, shows the total energy (internal and gravitational) profile as a function of the radial coordinate, ~~for the same example planet.~~ **Two choices: (1) define this cumulative energy more clearly and give it a different symbol than E_{tot} that's already used, maybe**

$E(r)$, or (2) plot the local (noncumulative) quantity epr^3 , which should peak in the interesting places. The bulk of the energy is concentrated deep in the atmosphere for the realistic EOS at high temperatures (3) and the fully realistic EOS curve (4), which shows that hydrogen dissociation in the inner atmosphere dictates the energy behavior of the envelope. In contrast, energy is concentrated towards the outer boundary for the $\nabla_{\text{ad}} = 0.3$ polytrope (1). **The key question here is how does the slope of the energy affect the quantity that matters, $|dE/dM|$? This is not clear yet. I think the shift to lower temperatures, seen in the $T(r)$ plot is helpful, but perhaps the EOS plots should also include an internal energy map.** Qualitatively, this can be explained through a simple analytic argument: the density profile in an adiabatic, non-self-gravitating atmosphere composed of an ideal gas scales as $\rho(r) \sim r^{1/\nabla_{\text{ad}}-1}$ (see Paper I) (The sign is wrong here and the error propagates to the energy. Should be \propto not \sim .) Since the total energy scales as $E(r) \sim \rho(r)r^2 \sim r^{1/\nabla_{\text{ad}}+1}$, (This is a new/contradictory use of E , what is given here is $dE/d\ln(r)$. Scaling is wrong as noted above. Again \propto not \sim .) adiabats with lower ∇_{ad} have their energy more tightly packed towards the interior of the envelope, which is the case during dissociation when ∇_{ad} decreases significantly (see Section §3 and Figure 1). It takes more energy to bring gas deep into the atmosphere for an envelope that has the bulk of its energy concentrated towards the bottom, (This argument isn't clear, new gas isn't brought deep into the atmosphere, it is added at the surface.) which increases the amount of energy per unit mass that needs to be radiated, i.e. $|dE/dM|$. The cooling time is therefore larger **with dissociation** for the realistic EOS at high temperatures (3) when compared to the ideal gas polytrope (1). This increase in $|dE/dM|$ is shown in the bottom-right panel of Figure 3.

We have seen that quantum rotational states transitions due to the low temperatures at the top of the atmosphere (already too long and convoluted) increase the thickness of the radiative zone, and decrease the luminosity of the envelope, while dissociation at high temperatures deep in the atmosphere increases the amount of energy needed to increase the atmosphere mass by a fixed amount. **Way too long a sentence!** Overall, both effects result in a longer time for the atmosphere to evolve.

5. OPACITY EFFECTS ON ATMOSPHERE EVOLUTION

So far in our model we have assumed that the dust opacity in the radiative region of the atmosphere is given by the standard ISM opacity. However, our scenario of low planetesimal accretion is likely to favor lower dust opacities, due to grain growth and dust settling. Grain growth, in particular, changes the particle size distribution when compared to the standard ISM size distribution (e.g., Pollack et al. 1985) and lowers the absolute value of the opacity. Enhanced metallicity due to planetesimal accretion, by construction not present during our atmosphere's growth, cannot make up for this reduction.

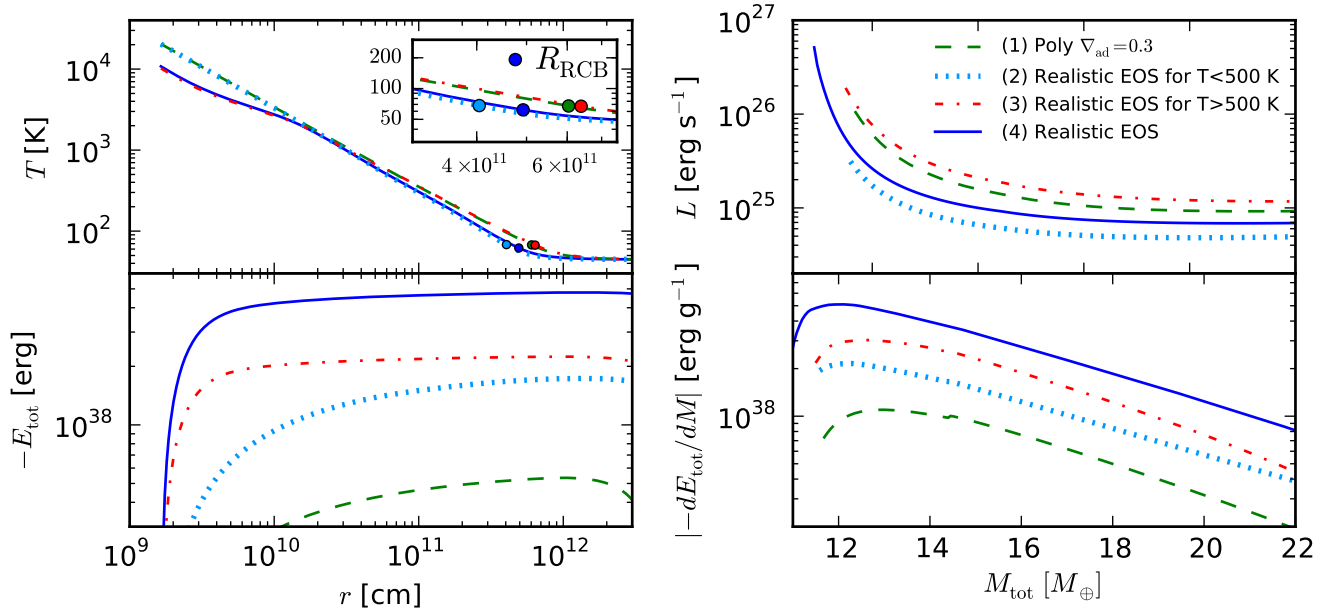


FIG. 3.— (Left and right panels could be different figs. The left panel could benefit from showing P or ρ . Also E_{tot} is not yet well defined; the local quantity e_{pr}^3 might be more instructive. A greater range of E would show what the polytrope is doing better. The right panel could benefit from adding M . We call $E_{\text{tot}} \rightarrow E$ elsewhere, so should be consistent. Why don't x-axes line up in right panel, are masses different? What is the discontinuity in dE/dM for the polytrope around $14 M_{\oplus}$? (A kink would be coarse resolution, but a discontinuity is harder to understand.) I don't think you need an abs. val. around $-dE/dM$.) We explore atmosphere growth around a core of $M_c = 10 M_{\oplus}$ forming at 10 AU in our fiducial disk, for the EOS choices in Figure 2. Upper-left panel: Instantaneous temperature profile as a function of the radial coordinate when the total mass (core + atmosphere) is $12 M_{\oplus}$. The location of the RCB is marked. Quantum rotational states at low temperatures in the outer region of the atmosphere result in a deeper RCB. Upper-right panel: Luminosity evolution as a function of total mass. Quantum rotational effects at low temperatures near the top of the atmosphere result in a lower luminosity for the realistic EOS (see text). Lower-left panel: Instantaneous energy profiles as a function on radius for a total mass of $12 M_{\oplus}$. Hydrogen dissociation deep in the atmosphere causes the bulk of the energy to be concentrated at the bottom of the envelope. This increases the amount of energy per unit mass that needs to be radiated away (dE/dM) resulting in a longer crossover time for the realistic EOS when compared to the polytrope. Lower-right panel: $|dE/dM|$ evolution as a function of total mass. Hydrogen dissociation deep in the atmosphere results in the bulk of the energy being concentrated at the bottom of the envelope, which increases the energy per unit mass that has to be radiated away when compared to an ideal gas polytrope. This results in slower growth.

Although grain growth and evidence for a non-ISM size distribution have been observed in protoplanetary disks (e.g., Beckwith et al. 1990, Beckwith & Sargent 1991, Pérez et al. 2012), the size distribution of dust particles has not been tightly constrained. Typically, the grain size distribution is assumed to be a power-law:

$$n(a) \sim a^{-p}, \quad (7)$$

where $n(a)$ is the number density of particles of size a and $p = 3.5$ (corresponding to a “normal” collisional cascade) or $p = 2.5$ (an approximation for coagulation). In this work we use the D’Alessio et al. (2001) frequency-dependent opacity tables to obtain the temperature-dependent Rosseland mean opacity κ . We take as a fiducial case a maximum particle size of 1 cm and a grain size distribution given by Equation (7) with $p = 3.5$. Other choices for the power-law coefficient p are discussed later in this section.

The D’Alessio et al. (2001) opacities are only relevant at temperatures that are sufficiently low for dust grains to remain solid ($T \lesssim 1000$ K). In the temperature regime where dust sublimates we use the Bell & Lin (1994) analytic opacity laws, ensuring smooth transition from the grain growth opacities.

The sharp drop in opacity ($\kappa \sim T^{-24}$, see Figure 15) due to dust sublimation lowers the radiative temperature gradient significantly (see Equation 3), and may therefore generate radiative layers within the inner region of the atmosphere (see Appendix C, Figure 15). This could in principle pose challenges for our model, since the additional luminosity generated in these radiative windows may be large enough to make our assumption of constant luminosity throughout the radiative layers invalid. In practice, however, the inner radiative windows are either very thin (Figure 15, middle panel), or the temperature gradient is flat enough to result in a roughly constant luminosity throughout the region (Figure 15, bottom panel; also see Equation 2c). This results in a negligible extra luminosity generated in the radiative windows. However, the radiative windows may become non-negligible for other opacity choices and sufficiently low core masses, as we show later in this section. We note that despite the existence of one or more radiative windows in the planet’s atmosphere, the luminosity that emerges at the outer boundary is set by the outer radiative layer. In fact, a simple estimate of the luminosity emerging at the RCB can be found as follows.

The equation of radiative diffusion (2c) can be approximated in terms of the radiative flux \mathcal{F} as

$$\mathcal{F} \sim \frac{\sigma T_{\text{RCB}}^4}{\tau}, \quad (8)$$

where τ is the optical depth of the upper radiative layer. Furthermore, we find that τ is dominated by the optical depth of the first scale height, i.e.

$$\tau \sim \tau_{\text{RCB}} = \kappa_{\text{RCB}} \rho_{\text{RCB}} H_{\text{RCB}}, \quad (9)$$

with

$$H_{\text{RCB}} = \frac{k_B T_{\text{RCB}}}{\mu m_p} \frac{R_{\text{RCB}}^2}{GM_{\text{RCB}}}, \quad (10)$$

where μ is the mean molecular weight of the gas, m_p the proton mass, and all other quantities are evaluated at the RCB. By substituting Equations (10) and (9) into Equation (8), and noting that $\mathcal{F} = L/(4\pi(R_{\text{RCB}} + H_{\text{RCB}})^2) \approx L/(4\pi R_{\text{RCB}}^2)$, we recover Equation (3) applied at the boundary between the uppermost convective region of the atmosphere and the outer radiative layer (where $\nabla_{\text{rad}} = \nabla_{\text{ad}}$) as

$$L \sim \frac{4\pi\sigma T_{\text{RCB}}^3 GM_{\text{RCB}} \mu m_p}{k_B \kappa_{\text{RCB}} \rho_{\text{RCB}}}. \quad (11)$$

Equation (11) can be used to estimate the luminosity emerging at the top of the convective layer of the atmosphere. We have verified that the luminosity emerging at the bottom of the outer radiative layer in our models can indeed be approximated by Equation (11).

Due to the variable number and position of radiative windows, and therefore radiative-convective boundaries, within the planet atmosphere, we cannot consistently calculate the time evolution of different atmospheres if we evaluate our cooling Equation (6) at the RCB, as we do in our standard model. We choose to evaluate the cooling time at the Bondi radius instead (since our cooling model applies at any radius R , see section §2.2). We note that our choice of R does not change the estimate of the atmosphere evolution time, to order of magnitude, since the additional luminosity generated in all radiative regions is negligible for our opacity choice (also see Paper I).

6. CRITICAL CORE MASS

In this section we put together the results obtained in Sections §4 and §5, and determine the minimum core mass to initiate runaway gas accretion during the lifetime of the protoplanetary disk, i.e. the critical core mass. As in Paper I, we quantify the runaway growth timescale t_{run} as the time at which the atmosphere growth time M_{atm}/\dot{M} drops to 10% of its maximum value (see Paper I for details). We first explore the dependence of the runaway growth time on the core mass for a fixed semimajor axis. We then determine the critical core mass to form a giant planet from a gas composed of a realistic hydrogen-helium mixture, and we compare this with the results from Paper I for an ideal diatomic gas. Finally, we determine the critical core mass under more realistic opacity assumptions.

Figure 4 displays the time evolution and the runaway growth time for atmospheres forming around cores with masses between $10 M_{\oplus}$ and $20 M_{\oplus}$ at $a = 10$ AU in our

fiducial disk. Higher mass cores have both shorter t_{run} and fractionally larger atmosphere masses at runaway, consistent with the results of Paper I.

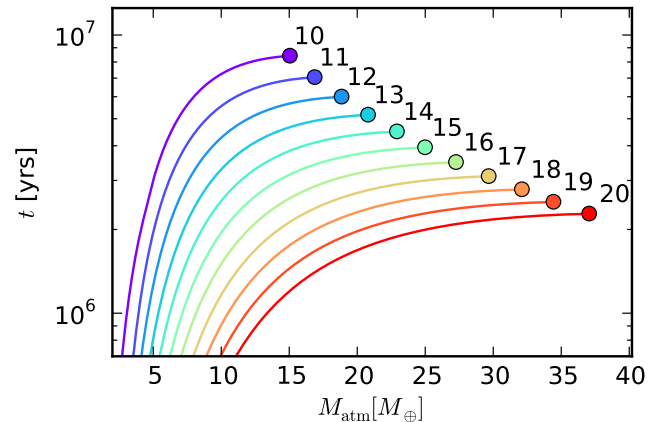


FIG. 4.— Elapsed time as a function of atmosphere mass, for cores with fixed masses between $10 M_{\oplus}$ and $20 M_{\oplus}$ at $a = 10$ AU in our fiducial disk. The circles mark the runaway growth time. The numbers are labeling the core mass in Earth masses. A larger core mass results in a lower t_{run} and a higher M_{atm}/M_c at runaway.

Figure 5 shows the critical core mass for a massive atmosphere to form during a typical lifetime of a protoplanetary disk $t = 3$ Myrs (e.g., Jayawardhana et al. 1999), for a gas described by a realistic EOS and an ISM dust opacity given by Equation (5) with $F_{\kappa} = 1$ and $\beta = 2$. The results of Paper I for an ideal diatomic gas are plotted for comparison. The use of a realistic EOS results in a critical core mass more than twice as large as that produced by a polytrope. As such, non-ideal effects substantially increase the core mass needed to form a giant planet before the dissipation of the protoplanetary disk.

Figure 6 shows the critical core mass as a function of semimajor axis, for a grain growth opacity with a size distribution given by the power-law (7) with $p = 3.5$ and maximum particle size of 1 cm. The critical core mass is lower than in the standard case, and less sensitive to location in the disk, i.e. the boundary conditions (temperature and pressure). We have shown in Paper I that the critical core mass is highly dependent on disk temperature rather than pressure. The temperature dependence, however, is mainly due to opacity. For the simplified analytic model developed in Paper I we found that the crossover time $t_{\text{co}} \sim T_{\text{d}}^{\beta+1/2}$, with β the power-law exponent in Equation (5) and t_{co} a proxy for t_{run} , defined as the time when $M_{\text{atm}} = M_c$, as t_{run} cannot be determined self-consistently for the analytic model. Opacity is less sensitive to temperature variations for larger grains and has an almost flat profile (see Figure 14), which results in $\beta \ll 1$ and a much weaker temperature (and therefore semimajor axis) dependence of the critical core mass, as seen in Figure 6. Moreover, grain growth reduces the absolute value of the opacity, which results in an overall lower runaway accretion time and critical core mass.

So far we have assumed that the size distribution of dust grains is a power-law (7) with $p = 3.5$ which corresponds to a normal collisional cascade. If, however,

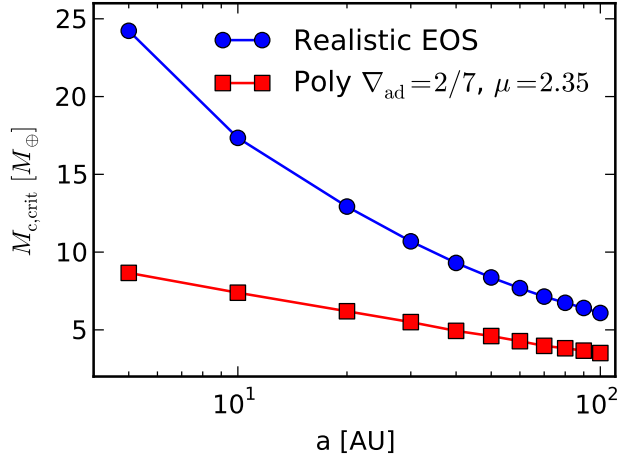


FIG. 5.— The minimum core mass for an atmosphere to initiate runaway gas accretion within the lifetime of a typical protoplanetary disk $t \sim 3$ Myrs as a function of semimajor axis, for a realistic hydrogen-helium mixture and a standard ISM power-law opacity. The results of Paper I for an ideal diatomic gas are plotted for comparison. The realistic EOS yields core masses larger by more than a factor of 2 when compared to the polytrope.

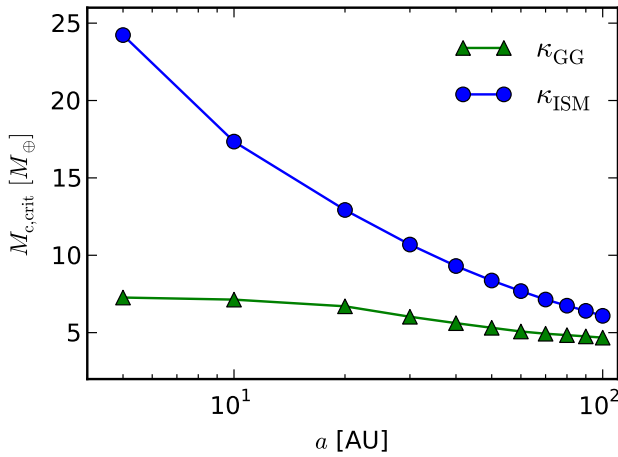


FIG. 6.— Critical core mass as a function of semimajor axis for radiative opacities that account for grain growth (green triangles, with $p = 3.5$ and $a_{\max} = 1$ cm; see text for details). The critical core mass is lower than it would be if dust grains had an ISM-like size distribution (blue circles).

coagulation is taken into account, the exponent p can be approximated as $p = 2.5$ (D’Alessio et al. 2001). This results in a flatter and significantly lower opacity, which may substantially reduce the critical core mass. However, we have found that our model breaks down for low core masses ($M_c \lesssim 3M_\oplus$) under our assumption of constant luminosity in the outer radiative layer. Figure 7 shows the crossover time t_{co} as a function of semimajor axis for the lowest core mass for which our model is valid, $M_c = 4M_\oplus$. The crossover time is more than one order of magnitude lower for $p = 2.5$, which implies that the critical core mass may be, in fact, significantly lower than presented in Figure 6.

7. EFFECTS OF PLANETESIMAL ACCRETION

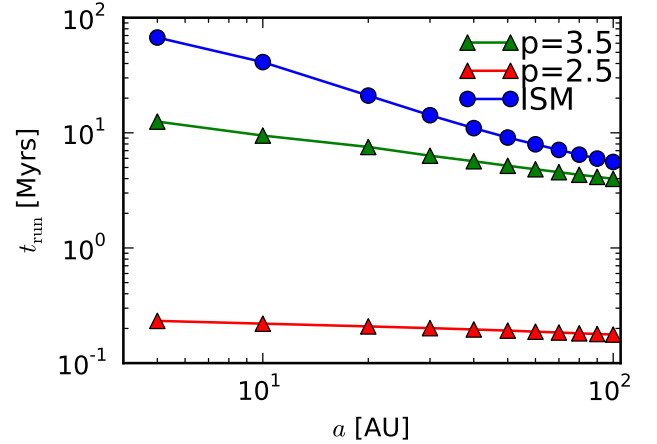


FIG. 7.— Runaway accretion times for different grain size distributions, for an atmosphere forming around a core with $M_c = 4M_\oplus$. The lines marked by green and red triangles have grain growth opacities with $a_{\max} = 1$ cm, and $p = 3.5$ and $p = 2.5$, respectively (see text for details). The blue circle line has an ISM power-law opacity. The runaway accretion time is more than one order of magnitude lower when coagulation is accounted for, i.e. $p = 2.5$.

In this study we have considered protoplanets with fully formed cores for which planetesimal accretion is negligible and KH contraction dominates the luminosity evolution of the atmosphere. This is different from calculations that assume high planetesimal accretion rates and find that the atmosphere is in steady state and solely heated due to accretion of solids. In this section we compare our results for the critical core mass to analogous results from steady-state fast planetesimal accretion calculations. We discuss the core accretion rates that are necessary for our regime to be valid in §7.1. In §7.2, we estimate core growth during atmosphere evolution at the maximum rate for which the KH regime is valid, and show it is negligible. Finally, we compare our results with those assuming fast planetesimal accretion in §7.3.

7.1. Planetesimal Accretion Rates

Kelvin-Helmholtz contraction dominates an atmosphere’s luminosity if $L_{\text{acc}} < L_{\text{KH}}$, where L_{acc} is the accretion luminosity,

$$L_{\text{acc}} = G \frac{M_c \dot{M}_c}{R_c}, \quad (12)$$

and L_{KH} is given by Equation (6) with $L_c = \Gamma = 0$. This condition is satisfied as long as the planetesimal accretion rate

$$\dot{M}_c < \dot{M}_{c,\text{KH}} \equiv \frac{L_{\text{KH}} R_c}{G M_c}. \quad (13)$$

To illustrate the magnitude of $\dot{M}_{c,\text{KH}}$, we choose as a fiducial case an atmosphere forming at 10 AU and with a core mass of $10M_\oplus$. Since analytic studies of critical core masses at high planetesimal accretion rates assume an ideal gas EOS, for ease of comparison we choose an ideal gas polytrope with constant adiabatic gradient $\nabla_{\text{ad}} = 2/7$ and mean molecular weight $\mu = 2.35$ (see also Paper I). For this choice of parameters, the runaway

accretion time is $t_{\text{run}} \sim 1.3$ Myrs, which is within the typical lifetime of a protoplanetary disk. We also estimate two reference accretion rates. The first one is the core accretion rate $\dot{M}_{c,\text{acc}}$ needed to grow the core to $M_c = 10M_\oplus$ on the same timescale as our model atmosphere, $\tau = 1.3$ Myrs:

$$\dot{M}_{c,\text{acc}}(M_c) \equiv \frac{M_c}{\tau}. \quad (14)$$

The second reference planetesimal accretion rate is $\dot{M}_{c,\text{Hill}}$, a typically assumed planetesimal accretion rate for which the random velocities of the planetesimals are of the order of the Hill velocity around the protoplanetary core (for a review, see Goldreich et al. 2004). Following R06 (equation A1),

$$\dot{M}_{c,\text{Hill}} = \Omega \Sigma_p R_c R_H, \quad (15)$$

where Σ_p is the surface density of solids, assumed to satisfy $\Sigma_d \approx 100\Sigma_p$ for a dust-to-gas ratio of 0.01.

Figure 8 shows that $\dot{M}_{c,\text{KH}}$ is $\sim 2 - 3$ orders of magnitude lower than $\dot{M}_{c,\text{acc}}$. Had the core accreted planetesimals at the $\dot{M}_{c,\text{KH}}$ rate since it started forming, it could not have grown large enough to attract an atmosphere within typical disk lifetime. This is consistent with the results of Pollack et al. (1996), which find that the planetesimal accretion rate decreases with time as the core's feeding zone is depleted, and with the requirement of our model that the planetesimal accretion rate is initially large during core growth, then significantly reduces as the gaseous envelope accumulates. This is a plausible scenario, as the core may have formed in the inner part of the disk and was later scattered outwards (Ida et al. 2013), or the planet's feeding zone could have been depleted of solids due to a giant neighbor.

7.2. Core Growth during KH Contraction

Planetesimal accretion during the KH contraction phase of atmosphere growth at a rate $\dot{M} < \dot{M}_{c,\text{KH}}$ cannot alter the core mass enough to affect the time evolution of the atmosphere. We can quantitatively estimate the increase in core mass as

$$\Delta M_c = \int_0^{t_{\text{run}}} \dot{M}_c dt \approx \sum_i \dot{M}_{c,i} \Delta t_i, \quad (16)$$

where the accretion rate $\dot{M}_{c,i}$ is given by

$$\dot{M}_{c,i} = \frac{L_i R_c}{GM_c} \quad (17)$$

from Equation (12), with L_i the luminosity of the atmosphere at time t_i in our model. For $M_c = 10M_\oplus$, we find $\Delta M_c \approx 0.05M_\oplus \ll 10M_\oplus$. It follows that a significant increase in core mass that could potentially alter the time evolution of the atmosphere would occur on a much longer timescale than the crossover time for the unperturbed atmosphere. The time evolution of the atmosphere is thus insensitive to core mass changes at a rate imposed by the assumption that $L_{\text{acc}} < L_{\text{KH}}$.

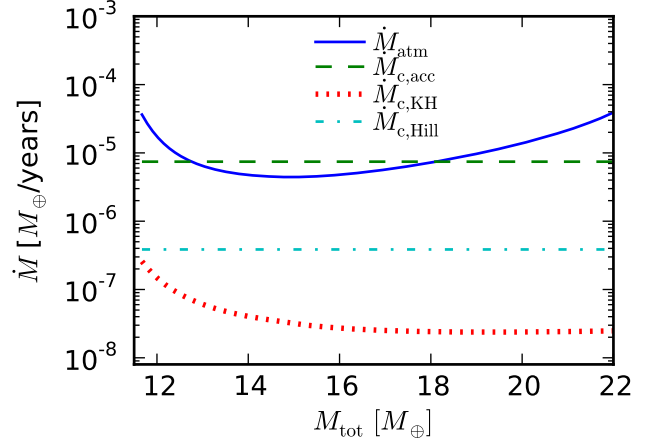


FIG. 8.— Various accretion rates for a planet forming at 10 AU and with a core mass $M_c = 10M_\oplus$, using a polytropic EOS and ISM power-law opacity. For this choice of parameters, the runaway accretion time is $t_{\text{run}} \sim 1.3$ Myrs. The \dot{M}_{atm} (solid blue) curve represents the growth rate of the atmosphere as estimated by our model. The core accretion rate $\dot{M}_{c,\text{acc}}$ (dashed green) necessary to grow the core on the timescale t_{run} is larger than $\dot{M}_{c,\text{KH}}$ (dotted red), the maximum planetesimal accretion rate during KH contraction for which our regime is valid (see text). The $\dot{M}_{c,\text{acc}}$ rate is also larger than the frequently used planetesimal accretion rate $\dot{M}_{c,\text{Hill}}$ (dashed-dotted light blue) for which the random velocity of the planetesimals is given by the Hill velocity due to the core (see text). This motivates our requirement that planetesimal accretion must have slowed down after core growth for our model to be valid.

7.3. Comparison with Steady-State Results

We compare our results for the critical core mass M_{crit} with those of studies that assume large planetesimal accretion rates. These studies find that the atmosphere is in steady state at all times and that static solutions only exist up to a maximum core mass, which they define as the critical core mass. If the M_{crit} found by static studies were lower than the M_{crit} in our regime of negligible solids accretion, the atmosphere would undergo runaway gas accretion before KH contraction became dominant, and our regime would not be relevant. We show, however, that our model yields lower core masses than those found when fast planetesimal accretion is considered.

In static studies, the critical core mass is larger for higher planetesimal accretion, as additional heating increases the core mass required for collapse. As such, if atmosphere collapse does not occur due to planetesimal accretion for the lowest value of $\dot{M}_{c,\text{KH}}$ over the course of the atmosphere's growth (see, e.g., Figure 8), then it can only occur in the KH dominated regime.

In order to estimate the critical core mass $M_{\text{crit,KH}}$ corresponding to planetesimal accretion at the rate $\dot{M}_{c,\text{KH}}$, we use the results of R06 for low luminosity atmospheres forming in the outer disk ($> 2 - 5$ AU), consistent with our region of interest. R06 assumes an ideal gas polytropic EOS and a lower opacity than the standard ISM (see Equation 5). We thus calculate the critical core mass for an ideal gas polytrope with the normalization factor F_κ reduced by a hundred, which is comparable to the

opacity law used by R06 ².

Following R06, we find that the critical core mass when accretion luminosity dominates the evolution of the atmosphere can be expressed as

$$M_{\text{crit,KH}} \sim \left[\frac{\min[\dot{M}_{\text{c,KH}}(M_c)]}{64\pi^2 C} \frac{\kappa_0}{\sigma G^3} \frac{1}{R_c M_c^{1/3}} \left(\frac{k_b}{\mu} \right)^4 \right]^{3/5}, \quad (18)$$

with C an order unity constant depending on the adiabatic gradient and disk properties (see R06, Equation B3). From Equation (13), the accretion rate $\dot{M}_{\text{c,KH}}$ depends on the core mass M_c . We find $M_{\text{crit,KH}}$ numerically by setting $M_c = M_{\text{crit,KH}}$ on the right-hand side of Equation (18). The result is displayed in Figure 9; the critical core mass corresponding to planetesimal accretion at the rates displayed in Figure 8 is displayed for comparison.

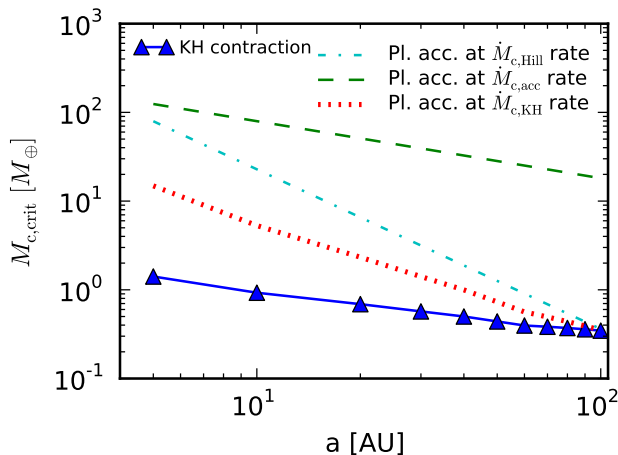


FIG. 9.— Comparison between the critical core mass $M_{\text{crit,KH}}$ given significant planetesimal accretion and the critical core mass when gas contraction dominates. Our results yield lower core masses than in the fast planetesimal accretion case (e.g., Rafikov 2006). The critical core mass corresponding to $\dot{M}_{\text{c,Hill}}$ and $\dot{M}_{\text{c,acc}}$ from Figure 8 is plotted for comparison.

The critical core mass in the regime where KH contraction dominates is smaller than in the case in which planetesimal accretion dominates the evolution of the atmosphere. This leads to two conclusions:

1. Planetesimal accretion can be safely ignored in our regime.
2. Giant planets can form from smaller cores if planetesimal accretion significantly reduces during at-

mosphere growth.

As additional heating due to planetesimals limits the atmosphere's ability to cool, our result represents a true minimum for the core mass needed to form a gas giant during the lifetime of the protoplanetary disk.

8. SUMMARY

In this paper we study the formation of giant planets embedded in a gas disk. We consider atmosphere evolution around fully grown cores and determine the minimum (critical) core mass required to form a gas giant during the typical lifetime of a protoplanetary disk. We improve the model developed in Piso & Youdin (submitted, hereafter Paper I) by including realistic equation of state (EOS) tables and dust opacities.

For a realistic EOS and grain growth opacity with maximum particle size $a_{\text{max}} = 1$ cm and a power-law size distribution (7) with $p = 3.5$, the critical core mass is $\sim 7M_{\oplus}$ at 5 AU in our fiducial disk and drops to $\sim 4.5M_{\oplus}$ at 100 AU. This result for the critical core mass M_{crit} is similar to the one obtained in Paper I for an ideal gas polytropic EOS and interstellar opacity. The realistic EOS and grain growth opacity have two competing effects on M_{crit} :

- Realistic EOS effects increase M_{crit} by a factor of ~ 2 when compared to the ideal gas polytrope.
- Grain growth opacities decrease M_{crit} by a factor of ~ 3 at 5 AU and by a factor of ~ 1.5 at 100 AU, when compared to ISM opacities, for a particle distribution given by the power-law (7) with $p = 3.5$ and a maximum particle size of 1 cm. The critical core mass is less sensitive to the location in the disk when realistic opacities are used. If $p = 2.5$, an approximation for coagulation, M_{crit} further reduces.

Our results yield lower core masses than analogous results that consider high planetesimal accretion rates for which the core and atmosphere grow simultaneously. It is thus possible to form a giant planet from a smaller core if the core grows first, then the accretion rate of solids is reduced and a gaseous envelope is accumulated. Moreover, since additional heat sources such as planetesimal accretion limit the ability of the atmosphere to cool and undergo Kelvin-Helmholtz contraction, our results represent a true minimum on the core mass needed to form a giant planet during the typical lifetime of a protoplanetary disk.

We thank Sean Andrews for providing us with the D'Alessio et al. (2001) opacity tables. We also thank Eugene Chiang and Steven Cranmer for useful conversations. ANY thanks Phil Arras for a methodical explanation of entropy.

REFERENCES

- Beckwith, S. V. W. & Sargent, A. I. 1991, *ApJ*, 381, 250
- ² The power-law opacity of R06 is scaled to the (semimajor axis dependent) disk temperature, while our opacity is scaled to an absolute reference temperature. We thus cannot directly use the R06 opacities for our comparison.
- Beckwith, S. V. W., Sargent, A. I., Chini, R. S., & Guesten, R. 1990, *AJ*, 99, 924
- Bell, K. R. & Lin, D. N. C. 1994, *ApJ*, 427, 987
- Blanksby, S. J. & Ellison, G. B. 2003, *Acc. Chem. Res.*, 36, 255
- Bodenheimer, P. & Pollack, J. B. 1986, *Icarus*, 67, 391
- Chiang, E. & Youdin, A. N. 2010, *Annual Review of Earth and Planetary Sciences*, 38, 493
- D'Alessio, P., Calvet, N., & Hartmann, L. 2001, *ApJ*, 553, 321

- D'Angelo, G., Durisen, R. H., & Lissauer, J. J. Giant Planet Formation, ed. S. Piper, 319–346
- Farkas, A. 1935, Orthohydrogen, Parahydrogen and Heavy Hydrogen
- Goldreich, P., Lithwick, Y., & Sari, R. 2004, ARA&A, 42, 549
- Ida, S., Lin, D. N. C., & Nagasawa, M. 2013, ApJ, 775, 42
- Ikoma, M., Nakazawa, K., & Emori, H. 2000, ApJ, 537, 1013
- Jayawardhana, R., Hartmann, L., Fazio, G., Fisher, R. S., Telesco, C. M., & Piña, R. K. 1999, ApJ, 521, L129
- Kippenhahn, R. & Weigert, A. 1990, Stellar Structure and Evolution
- Kittel, C., Kroemer, H., & Landsberg, P. T. 1981, Nature, 289, 729
- Langmuir, I. 1912, J. Am. Chem. Soc., 34, 860
- Mandl, F. 1989, Statistical Physics, 2nd Edition
- Mizuno, H., Nakazawa, K., & Hayashi, C. 1978, Progress of Theoretical Physics, 60, 699
- Ormel, C. W. 2013, MNRAS, 428, 3526
- Papaloizou, J. C. B. & Nelson, R. P. 2005, A&A, 433, 247
- Papaloizou, J. C. B. & Terquem, C. 1999, ApJ, 521, 823
- Pérez, L. M., Carpenter, J. M., Chandler, C. J., Isella, A., Andrews, S. M., Ricci, L., Calvet, N., Corder, S. A., Deller, A. T., Dullemond, C. P., Greaves, J. S., Harris, R. J., Henning, T., Kwon, W., Lazio, J., Linz, H., Mundy, L. G., Sargent, A. I., Storm, S., Testi, L., & Wilner, D. J. 2012, ApJ, 760, L17
- Pollack, J. B., Hubickyj, O., Bodenheimer, P., Lissauer, J. J., Podolak, M., & Greenzweig, Y. 1996, Icarus, 124, 62
- Pollack, J. B., McKay, C. P., & Christofferson, B. M. 1985, Icarus, 64, 471
- Rafikov, R. R. 2006, ApJ, 648, 666
- Saumon, D., Chabrier, G., & van Horn, H. M. 1995, ApJS, 99, 713
- Semenov, D., Henning, T., Helling, C., Ilgner, M., & Sedlmayr, E. 2003, A&A, 410, 611
- Stevenson, D. J. 1982, Planet. Space Sci., 30, 755
- Thompson, M. J. 2006, An introduction to astrophysical fluid dynamics
- Vardya, M. S. 1960, ApJS, 4, 281

APPENDIX

EQUATION OF STATE TABLES

In this study we consider atmosphere growth in the outer parts of protoplanetary disks ($5 < a < 100$ AU), where temperature and pressure drop to as little as $T \sim 20$ K and $P \sim 10^{-4}$ dyn cm $^{-2}$ for our MMSN disk model (see equations 1b and 1c). We assume that the nebular gas is described by a realistic equation of state (EOS), as prescribed by the Saumon et al. (1995) EOS tables. However, these tables only cover a relatively high range of temperatures and pressures, i.e. $2.1 < \log_{10} T(\text{K}) < 7.06$ and $4.0 < \log_{10} P(\text{dyn cm}^{-2}) < 19.0$. We thus need to extend the tables to lower T and P , as required by our disk model. We calculate ∇_{ad} for

$$1.0 < \log_{10} T < 2.1 \quad (\text{A1})$$

$$-4.4 < \log_{10} P < 4.0 \quad (\text{A2})$$

$$(\text{A3})$$

using the following method.

Hydrogen

For a system of particles, the partition function can be written as the product of all partition functions associated with each type of internal energy:

$$Z = Z_t Z_r Z_v \quad (\text{A4})$$

where Z_t , Z_r , Z_v are the partition functions associated with translation, rotation, and vibration, respectively.³ Our derivations follow Kittel et al. (1981)

In the classical limit, the partition function associated with the motion of the center of mass of a gas molecule of mass m is given by:

$$Z_t = (m/2\beta\pi\hbar^2)^{3/2}V, \quad (\text{A5})$$

with T and V the gas temperature and volume, respectively, \hbar the reduced Planck constant, and $\beta = 1/(k_b T)$. The rotational partition function is generally written as:

$$Z_r = \sum_{j=0}^{\infty} (2j+1) \exp \left[\frac{-j(j+1)\Theta_r}{T} \right], \quad (\text{A6})$$

where Θ_r is the characteristic temperature for rotational motion. In the case of hydrogen, $\Theta_r \approx 85$ K. However, molecular hydrogen occurs in two isomeric forms: orthohydrogen, with the proton spins aligned parallel to each other, and parahydrogen, with the proton spins aligned antiparallel. Parahydrogen can only have symmetric (even) wave function associated with rotation, while orthohydrogen can only have an antisymmetric (odd) wave function associated with rotation. The rotational partition functions for ortho- and parahydrogen can thus be written as:

$$Z_{r,\text{para}} = \frac{1}{2} \sum_{j=0}^{\infty} (1 + (-1)^j) (2j+1) \exp \left[-\frac{j(j+1)\Theta_r}{T} \right] \quad (\text{A7})$$

³ We ignore electronic and nuclear excitation as they are only important at temperatures much higher than our regime of interest.

and

$$Z_{r,\text{ortho}} = \frac{3}{2} \sum_{j=0}^{\infty} (1 - (-1)^j)(2j+1) \exp \left[-\frac{j(j+1)\Theta_r}{T} \right] \quad (\text{A8})$$

The factor of 3 in Equation (A8) accounts for the three-fold degeneracy of the ortho state.

When the two isomers are in equilibrium, the combined partition function is given by the sum of the individual partition functions, $Z_r = Z_{r,\text{ortho}} + Z_{r,\text{para}}$ and can be written as:

$$Z_r = \sum_{j=0}^{\infty} (2 - (-1)^j)(2j+1) \exp \left[\frac{-j(j+1)\Theta_r}{T} \right] \quad (\text{A9})$$

In our range of temperatures of interest, we found that Z_r converges after about 25 terms in the series.

Finally, the partition function for vibrational motion is given by:

$$Z_v = [1 - \exp(\theta_v/T)]^{-1}, \quad (\text{A10})$$

where θ_v is the characteristic temperature for vibrational motion, $\theta_v \approx 6140$ K for hydrogen.

If the partition function of a system particles is known in terms of (V, T) , the internal energy per unit mass, entropy per unit mass and specific heat capacity can be written as

$$U = \mathcal{R}T^2 \left(\frac{\partial \log Z}{\partial T} \right)_V \quad (\text{A11})$$

$$S = \mathcal{R} \log Z + \frac{U}{T} \quad (\text{A12})$$

$$C_v = \left(\frac{\partial U}{\partial T} \right)_V. \quad (\text{A13})$$

Since $Z = Z_t Z_r Z_v$, we may write $U = U_t + U_r + U_v$ and $S = S_t + S_r + S_v$, where U_t , U_r , U_v , S_t , S_r , S_v are the quantities corresponding to the individual translation, rotation and vibration partition functions, respectively.

The entropy per mass due to translational motion can be expressed as:

$$S_t = \mathcal{R} \left[\frac{5}{2} \ln T - \ln P + \ln \left(\frac{(2\pi)^{3/2} \mathcal{R}^{5/2} \mu^4}{h^3} \right) + \frac{5}{2} \right] \quad (\text{A14})$$

with μ the mean molecular weight. Equation (A14) is known as the Sackur-Tetrode formula, and it is only applicable to an ideal gas. The internal energy per mass due to translational motion is given by:

$$U_t = \frac{3}{2} \mathcal{R}T \quad (\text{A15})$$

Putting all of the above together, we can now evaluate the thermodynamic quantities needed to extend the Saumon et al. (1995) EOS tables to low temperatures and pressures.

1. **Density.** In the low temperature, low pressure regime, hydrogen is molecular and behaves like an ideal gas. As such, the density in this region follows the ideal gas law $P = \rho \mathcal{R}T$.
2. **Internal energy per mass.** $U = U_t + U_r + U_v$, where U_t is given by Equation(A15), and U_r and U_v are determined using equations (A11), (A9) and (A10) above.
3. **Entropy per unit mass.** Similarly, $S = S_t + S_r + S_v$, where S_t is given by Equation (A14), and S_r and S_v can be determined from Equation (A12) and the calculated expressions for U_r and U_v , respectively.
4. **Entropy logarithmic derivatives.** The logarithmic derivatives S_T and S_P are given by:

$$S_T = \left. \frac{\partial \log S}{\partial \log T} \right|_P \quad (\text{A16})$$

and

$$S_P = \left. \frac{\partial \log S}{\partial \log P} \right|_T \quad (\text{A17})$$

We calculate S_T and S_P through finite differencing.

5. **Adiabatic gradient** ∇_{ad} . The adiabatic gradient is defined as:

$$\nabla_{\text{ad}} = \left. \frac{\partial \log T}{\partial \log P} \right|_S = -\frac{S_P}{S_T} \quad (\text{A18})$$

We evaluate it from the tabulated values for S_T and S_P determined above. Figure 10 shows a contour plot of ∇_{ad} as a function of temperature and pressure for the extended EOS table.

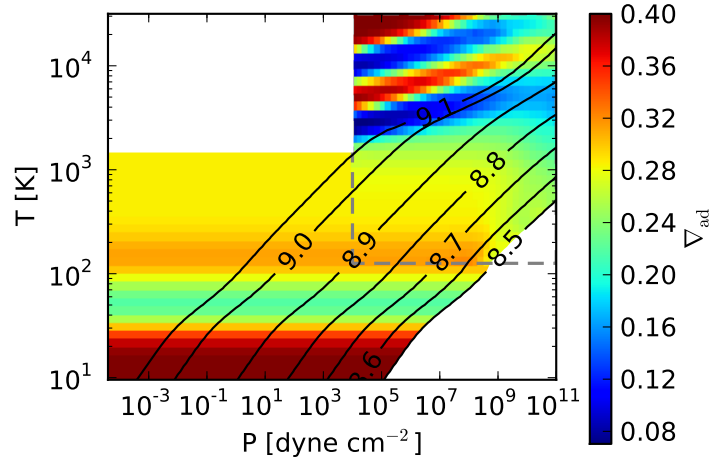


FIG. 10.— Contour plot of the hydrogen adiabatic gradient ∇_{ad} as a function of gas temperature and pressure. The upper right rectangle encloses the region described by the original Saumon et al. (1995) EOS tables, while the rest of the plot is our extension to lower temperatures and pressures. The black curves represent constant entropy adiabats, with the labels the natural logarithm of the absolute entropy per unit mass. At high temperatures, hydrogen dissociates and ionizes, while at low temperatures the rotational states of the hydrogen molecule are only partially excited and it no longer behaves like an ideal diatomic gas. Regions in which the EOS is invalid or has not been computed are masked in white (see Figure 1 caption for an explanation).

Helium

We extend the helium EOS tables based on a similar procedure. Since helium is primarily neutral and atomic at low temperatures and pressures, we treat it as an ideal monoatomic gas, and thus only take into account the translational component of the partition function (A5). Figure 11 shows ∇_{ad} as a function of temperature and pressure for the extended EOS table.

Lastly, we combine Figures 10 and 11 to obtain the EOS tables for the hydrogen-helium mixture thorough the procedure described in Saumon et al. (1995), for a helium mass fraction $Y = 0.3$ (Figure 1).

ADIABATIC GRADIENT VARIATIONS

Adiabatic Gradient during Partial Dissociation

The total internal energy of a partially dissociated gas includes contributions from the individual internal energies of the molecules and atoms, as well as from the dissociation energy. The dissociation energy depends on the dissociation fraction x (i.e., the fraction of molecules that have dissociated), which can be found from the Saha equation (see e.g., Kippenhahn & Weigert 1990, Chapter 14) as a function of temperature and density,

$$\frac{x^2}{1-x} \propto \frac{T^{3/2}}{\rho} e^{-\chi/k_B T}, \quad (\text{B1})$$

where $\chi=4.48$ eV is the dissociation energy for molecular hydrogen (Blanksby & Ellison 2003).

The above also holds true for ionization, with the dissociation energy replaced by ionization energy $\chi = 13.6$ eV for atomic hydrogen (Mandl 1989). From the Saha equation one can find an expression for ρ as a function of T and x , then derive the adiabatic gradient directly from its definition (Equation 4), taking into account the fact that the mean molecular weight in the ideal gas law varies with x , hence the pressure will not only be a function of T and ρ but also of x (see Kippenhahn & Weigert 1990, Chapter 14.3 for a detailed derivation). The final expression for the adiabatic gradient during ionization is

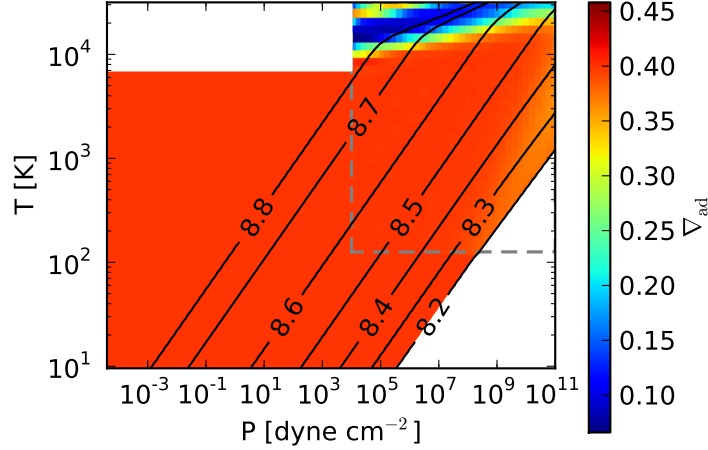


FIG. 11.— Contour plot of the helium adiabatic gradient ∇_{ad} as a function of gas temperature and pressure. The upper right rectangle encloses the region described by the original Saumon et al. (1995) EOS tables, while the rest of the plot is our extension to lower temperatures and pressures. The black curves represent constant entropy adiabats, with the labels the natural logarithm of the absolute entropy per unit mass. Helium ionizes at $T \gtrsim 10,000$ K, but behaves as an ideal monatomic gas otherwise. We choose $T = 7,000$ K as a conservative temperature cutoff above which our extension is no longer valid (masked in white). The EOS has not been computed in the lower-right region of the plot — see Figure 1 for an explanation.

$$\nabla_{\text{ad}} = \frac{2 + x(1-x)\Phi_H}{5 + x(1-x)\Phi_H^2}, \quad (\text{B2})$$

with $\Phi_H \equiv \frac{5}{2} + \frac{\chi}{k_B T}$. The derivation of ∇_{ad} during dissociation is more involved mathematically (see, e.g., Vardya 1960) and leads to a slightly more complicated final expression,

$$\nabla_{\text{ad}} = \frac{1 + x + \frac{x(1-x^2)}{2} \frac{\chi}{k_B T}}{5x + \frac{7(1-x)}{2} + \frac{x(1-x^2)}{2} \left(\frac{\chi}{k_B T} \right)^2}. \quad (\text{B3})$$

Using Equation (B3), we recover $\nabla_{\text{ad}} = 2/7$ for $x = 0$ (no ongoing dissociation hence hydrogen is purely molecular and diatomic) and $\nabla_{\text{ad}} = 2/5$ for $x = 1$ (hydrogen is fully dissociated into atoms and hence monatomic). Figure 12 shows the dependence of ∇_{ad} on the dissociation fraction, for $T = 3000$ K, the temperature at which dissociation typically occurs (Langmuir 1912). The adiabatic gradient drops substantially during partial dissociation, since part of the internal energy is used in dissociation rather than in increasing the temperature of the system.

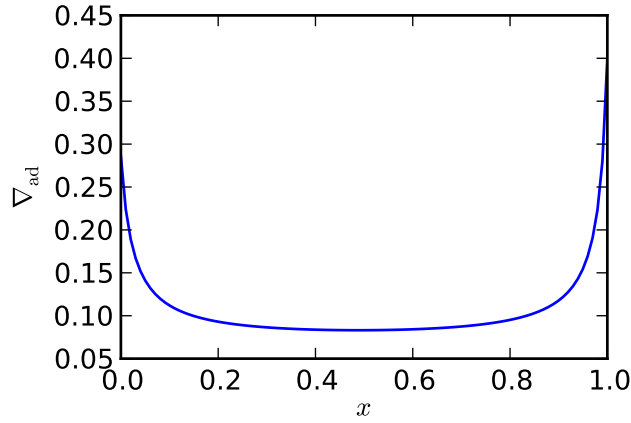


FIG. 12.— Adiabatic gradient as a function of the hydrogen dissociation fraction x . The adiabatic gradient is $\nabla_{\text{ad}} = 2/7$ for pure molecular hydrogen ($x = 0$) and $\nabla_{\text{ad}} = 2/5$ for fully atomic hydrogen ($x = 1$), and drops to low values during partial dissociation.

Adiabatic Gradient during Conversion of Spin Isomers

The adiabatic gradient scales as $\nabla_{\text{ad}} \sim 1/c_V = 1/(c_{V,t} + c_{V,r}) \sim 1/c_{V,r}$, where c_V is the specific heat capacity at constant volume, and $c_{V,t}$ and $c_{V,r}$ are the translational and rotational components, respectively. The second equality is due to the fact that $c_{V,t} = 3\mathcal{R}/2$ is independent of temperature. We can therefore understand how conversion between spin isomers affects ∇_{ad} by studying the dependence on temperature of $c_{V,r}$ of the ortho-para mixture.

The internal energy per unit mass and specific heat capacity associated with rotation for the individual isomers and for the equilibrium mixture can be derived from their partition functions (see Appendix A for details), and are plotted in Figure 13 (after Farkas 1935, Figure 1). At low temperatures, parahydrogen is in the $j = 0$ state and has no rotational energy, while orthohydrogen is in the $j = 1$ state and has the energy of its first rotational level. Both para- and orthohydrogen, as well as their equilibrium mixture, behave like monatomic gases at low temperatures and thus have zero rotational heat capacity. This is consistent with $\nabla_{\text{ad}} = 2/5$ at low temperatures as seen in Figure 1. As the temperature increases, the energetically higher-lying rotational states of para- and orthohydrogen are populated and the heat capacity of both spin isomers increases as a result. We note that the heat capacity of the equilibrium mixture is not a weighted average of the heat capacities of the individual components because it takes into account both the rotational energy uptake of para- and orthohydrogen, and also the shift in their equilibrium concentrations with temperature. This results in a peak in the heat capacity of the mixture around ~ 50 K, as seen in the bottom plot of Figure 13. As $\nabla_{\text{ad}} \sim 1/c_{V,r}$, it follows that the adiabatic gradient has to reduce, reach a minimum, then increase as the temperature rises, as shown in Figure 1.

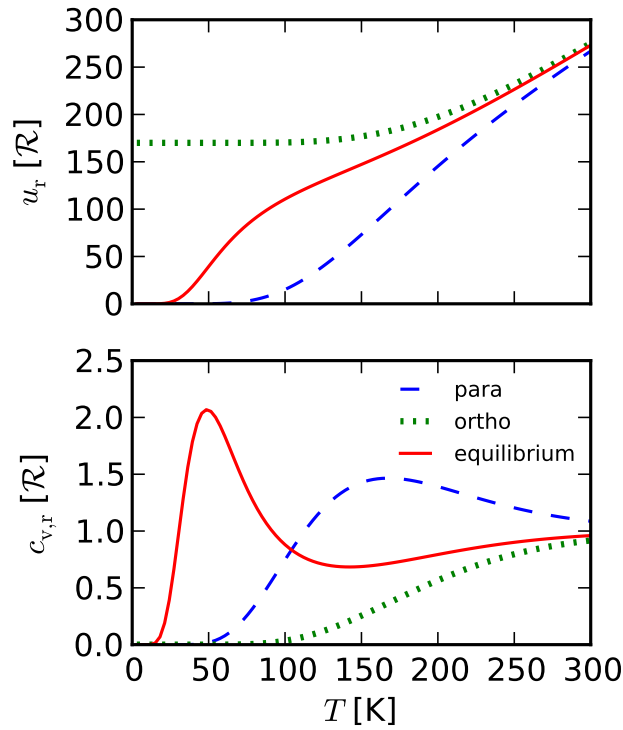


FIG. 13.— Internal energy per unit mass and specific heat capacity associated with rotation for parahydrogen (dashed blue), orthohydrogen (dotted green), and the equilibrium mixture (solids red) as a function of temperature. After Farkas (1935), Figure 1.

GRAIN GROWTH OPACITY AND RADIATIVE WINDOWS

The opacity of the interstellar medium is reasonably well constrained and approximate analytic expressions for the Rosseland mean opacity as a function of temperature and density are derived in Bell & Lin (1994). For low temperatures ($T \lesssim 100$ K) at which ice grains are present, opacity scales with temperature as $\kappa \sim T^2$. Sublimation of ice grains at ~ 150 K and of metal grains at ~ 1000 K results in sharp opacity drops. This is shown in Figure 14 for a gas density $\rho = 10^{-8}$ g cm $^{-3}$, which is typical for the outer regions of protoplanetary disks. Semenov et al. (2003) calculate Rosseland mean opacities in protoplanetary disks for grains of different sizes and structure. As shown in Figure 14, their results are in good agreement with Bell & Lin (1994). However, Semenov et al. (2003) do not take grain growth into account, which is likely to occur in protoplanetary disks, particularly at the late times when cores form. D'Alessio et al. (2001) compute wavelength dependent opacities for a range of maximum particle sizes and different size distributions. Figure 14 shows the integrated Rosseland mean opacity for a maximum particle size

of 1 cm and a power law size distribution $n \sim a^{-p}$, with a the grain size and $p = 3.5$ for a normal collisional cascade and $p = 2.5$ when coagulation is taken into account. We see in Figure 14 that this yields a mean opacity that is both lower and less sensitive to temperature, when compared to Bell & Lin (1994) or Semenov et al. (2003). However, observations of dust in protoplanetary disks have only been made at low temperatures (i.e., before dust sublimates). As we see in Figure 14, the opacity dramatically decreases during dust sublimation for ISM grains, which can result in regions in the inner parts of planetary atmospheres where energy is transported radiatively, i.e. radiative windows. We thus use the Bell & Lin (1994) opacities for $T \gtrsim 1000$ K, ensuring that they smoothly match the D'Alessio et al. (2001) opacities for lower temperatures.

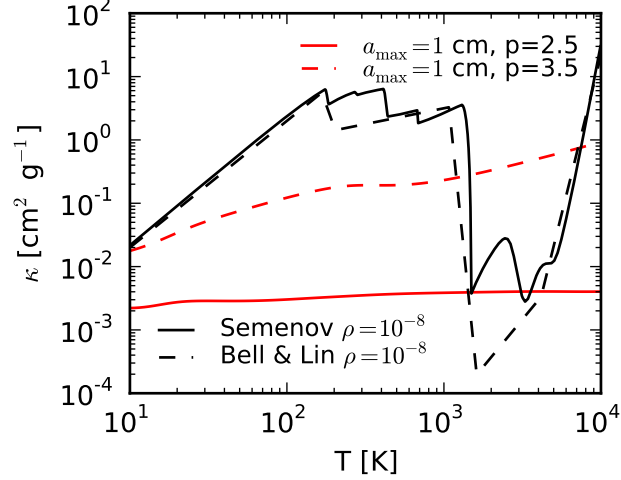


FIG. 14.— Rosseland mean opacity of dust grains as a function of temperature for different opacity assumptions. The dashed black curve shows the Bell & Lin (1994) analytic ISM opacity for $\rho = 10^{-8}$ g cm $^{-3}$. The solid black curve shows the tabulated opacity of Semenov et al. (2003) for a dust composition of 'normal' silicates. The dashed red curve shows the D'Alessio et al. (2001) opacity, which takes grain growth into account, for a maximum particle size of 1 cm and a standard collisional cascade grain size distribution ($p = 3.5$). The solid red curve is the same as the dashed red curve, but it accounts for coagulation ($p = 2.5$).

The significant opacity drop due to the sublimation of ice and metal grains lowers the radiative temperature gradient ∇_{rad} , which may result in one or more inner radiative layers inside the atmosphere of a protoplanet. This is displayed in Figure 15: depending on the semimajor axis and core mass, the opacity drop will generate no radiative window (top panel), one radiative window (middle panel), or two radiative windows (bottom panel).

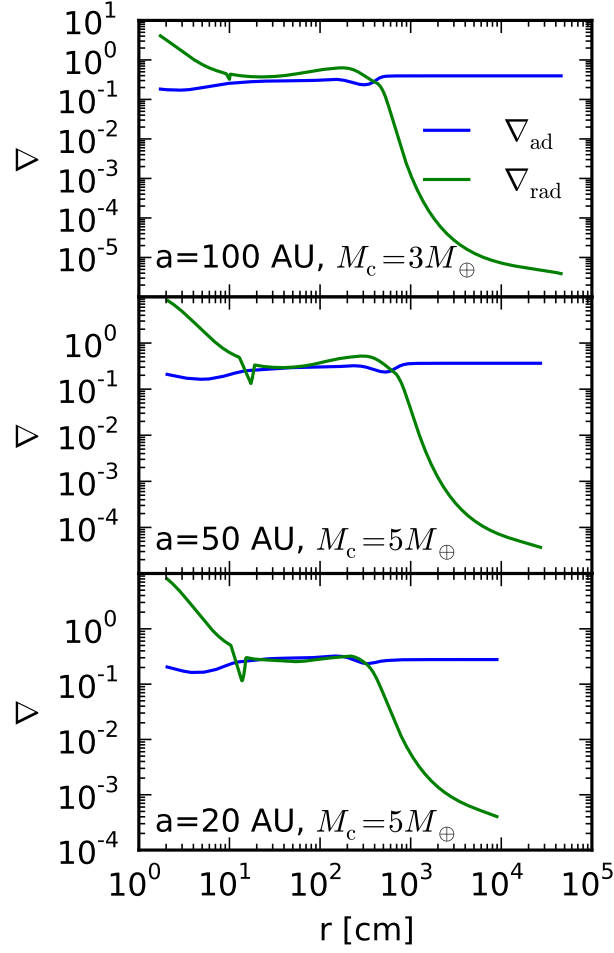


FIG. 15.— Snapshots of the radiative and adiabatic gradient as a function of the radial coordinate, for planets with different core masses forming at various locations in the disk. The nebular gas is described by a realistic EOS. The sharp drop in opacity due to dust sublimation may generate one or more radiative windows. Top panel: no radiative window for $a = 100$ AU and $M_c = 3M_{\oplus}$. Middle panel: the sharp opacity decrease produces one radiative window for $a = 50$ AU and $M_c = 5M_{\oplus}$. Bottom panel: the decrease in opacity results in two radiative windows for $a = 20$ AU and $M_c = 3M_{\oplus}$.